Med Biol Eng Comput (2014) 52:393–403
DOI 10.1007/s11517-014-1139-9

ORIGINAL ARTICLE

Extended Gabor approach applied to classification of emphysematous patterns in computed tomography

Rodrigo Nava · Boris Escalante-Ramírez · Gabriel Cristóbal · Raúl San José Estépar

Received: 22 February 2013 / Accepted: 16 January 2014 / Published online: 5 February 2014

Abstract Chronic obstructive pulmonary disease (COPD) is a progressive and irreversible lung condition typically related to emphysema. It hinders air from passing through airpaths and causes that alveolar sacs lose their elastic quality. Findings of COPD may be manifested in a variety of computed tomography (CT) studies. Nevertheless, visual assessment of CT images is time-consuming and depends on trained observers. Hence, a reliable computer-aided diagnosis system would be useful to reduce time and inter-evaluator variability. In this paper, we propose a new emphysema classification framework based on complex Gabor filters and local binary patterns. This approach simultaneously encodes global characteristics and local information to describe emphysema morphology in CT images. Kernel Fisher analysis was used to reduce dimensionality and to find the most discriminant nonlinear boundaries among classes. Finally, classification was performed using the *k*-nearest neighbor classifier. The results have shown the effectiveness of our approach for quantifying lesions due to emphysema and that the combination of descriptors yields to a better classification performance.

Keywords COPD · Emphysema · Gabor filters · Kernel Fisher analysis · Local binary patterns · Texture analysis

R. Nava (✉)
Posgrado en Ciencia e Ingeniería de la Computación, Universidad Nacional Autónoma de México, Mexico City, Mexico
e-mail: uriel.nava@gmail.com

B. Escalante-Ramírez
Departamento de Procesamiento de Señales, Facultad de Ingeniería, Universidad Nacional Autónoma de México, Mexico City, Mexico

G. Cristóbal
Instituto de Óptica, Spanish National Research Council (CSIC), Serrano 121, 28006 Madrid, Spain

R. S. J. Estépar
Brigham and Women's Hospital, Harvard Medical School, Boston, MA, USA

1 Introduction

COPD describes a collection of lung diseases that are characterized by parenchymal destruction and gradual limitation of airflow. Although it may manifest as emphysema, chronic bronchitis, or both, the former is the most common pathophysiological manifestation and is mainly attributable to tobacco smoking [2]. Studies of the World Health Organization report that over 65 million people have COPD worldwide and predict that it will be responsible for 10 % of the world's mortality by 2030 [22]. Therefore, in order to prevent other health complications such as pneumothorax and respiratory infections, the accurate characterization of emphysema is required for developing efficient treatments.

The literature recognizes three types of emphysema[26]: (1) **Paraseptal** (PS) also known as distal acinar emphysema is characterized by destruction of distal airway structures, alveolar ducts, and alveolar sacs. It is localized around the pleura; (2) **Panlobular** (PL) or panacinar emphysema destroys uniformly alveoli and prevails in the lower half of the lungs; and (3) **Centrilobular** (CL) or centriacinar emphysema is the most common type of pulmonary emphysema. It begins in the respiratory bronchioli and spreads peripherally. Most of the damage is usually contained to the upper half of the lungs.

Attenuation values in CT images, which are expressed in the Hounsfield unit (HU) scale, have been used to

identify pathological changes in lung parenchyma because they are linked to physical density of lung tissue [14]. Hayhurst et al. [9] showed that attenuation values in patients who had CL differed from healthy patients with normal tissue (NT).

Density mask is a common technique used to quantify emphysema. It describes the amount of air presented in a CT image and computes the percentage of pixel values smaller than a previously selected threshold. Routinely, −910 HU is taken as a standard threshold but recently Madani et al. [12] observed that if the threshold lies somewhere between −960 to −980, HU then the correlation with emphysema is larger. Mean lung density [25] is another objective measure of the extent of macroscopic emphysema; it is defined as the percentage of tissue lung below −950 HU. All these metrics consider that emphysema causes an abnormal enlargement of air spaces; thus, the air-tissue ratio in an emphysematous lung should increase, whereas the density should decrease proportionally to the amount of emphysema. Nevertheless, such methods are sensitive to scanner calibration and noise. In addition, they cannot distinguish emphysema patterns due to averaging effect.

On the other hand, texture analysis in lung CT images may provide new insights toward the construction of a reliable computer-aided diagnosis system because it is capable of identify changes in lung parenchyma and abnormalities associated with emphysema. For instance, Sørensen et al. [24] combined textural features using local binary patterns (LBPs) to classify three classes of emphysema. In [3], fractal analysis was proposed to classify 3258 emphysema patches of size 64 × 64 pixels. A simpler alternative based on the density estimation of local histograms was introduced in [13]. A different approach was presented in [23] where the authors used metadata to label lung samples. A technique based on the embedded probabilistic PCA was proposed in [29] to classify interstitial lung abnormalities that include emphysema as one class, whereas in [5], the Riesz transform was used to obtain features of lung abnormalities.

In this study, we propose a novel approach that exploits the advantages of complex Gabor filters (CGF) such as the strong correlation with the human visual system and simultaneously encodes local intensity information provided by LBPs. The former are global descriptors, whereas the latter are local operators. Since the low-attenuation areas in lung CT images describe different emphysema patterns, the discrimination problem was focused on the characterization of local intensities and global spatial variations. Our approach considers these aspects and provides a robust representation for each type of emphysema. Therefore, an improvement in the classification rate can be attained. We used a methodology composed of three stages to assign a given patch to one of several patterns: (1) feature extraction, (2) dimensionality reduction using kernel Fisher discriminant analysis (KFDA), and (3) classification using k-nearest neighbor (k-NN) classifier.

This paper is organized as follows: In Sect. 2, we described the construction of the feature vectors. In Sect. 3, we explained the procedure to reduce dimensionality. The data are presented in Sect. 4. The experiments and results are detailed in Sect. 5. Finally, our work is summarized in Sect. 6.

2 A bio-inspired model for feature extraction

In the mid-eighties, Daugman found out that the shape of Gabor functions and the psychophysical properties of simple receptive fields have a close match [4, 8, 10]. Furthermore, he proved that the conjoint time–frequency properties of 1D Gabor functions are still satisfied for the two-dimensional case.

2D Gabor functions, which are band-pass filters, occupy the smallest possible volume in the time–frequency space; such a volume represents the theoretical lowest bound of the uncertainty principle: $(\Delta x)(\Delta y)(\Delta u)(\Delta v) \geq \frac{1}{16\pi^2}$ where (x, y) and (u, v) correspond to spatial and frequency variables, respectively.

Gabor functions are defined as the product of a Gaussian function and a complex sinusoid and form a complete but non-orthogonal basis set, see (Fig. 1).

The canonical 2D Gabor function in the spatial domain is defined as:

$$g(x,y) = Ke^{-\frac{1}{2}\left[\frac{(x-x_0)^2+\gamma^2(y-y_0)^2}{\alpha^2}\right]+i(2\pi[u_0(x-x_0)+v_0(y-y_0)]+\phi)} \quad (1)$$

where $K = \frac{\gamma}{2\pi\alpha^2}$ is a normalizing constant, (x_0,y_0) represents the center of the function, (u_0, v_0) and ϕ are the central frequency and the phase of the sinusoidal signal, respectively. (α, γ) control the bandwidth of the Gaussian envelope along X- and Y-axes. We considered functions centered at the origin, $x_0 = 0$, $y_0 = 0$, and although the phase was implicitly encoded, it was ruled out in the present study.

Now, let us apply to (1) the Euler's formula, hence, we have the next expression:

$$g(x,y) = Ke^{-\frac{1}{2}\left(\frac{x^2+\gamma^2y^2}{\alpha^2}\right)}[\cos(2\pi u_0 x) + i\sin(2\pi u_0 x)] \quad (2)$$

The previous Eq. (2) can be divided into two parts, $g(x, y) = g_e(x, y) + ig_o(x, y)$, where

$$g_e(x,y) = Ke^{-\frac{1}{2}\left(\frac{x^2+\gamma^2y^2}{\alpha^2}\right)}\cos(2\pi u_0 x) \quad (3)$$

is an even-symmetric function, which responds with a maximum in zero. This property is suitable for detecting salient edges. On the other hand,

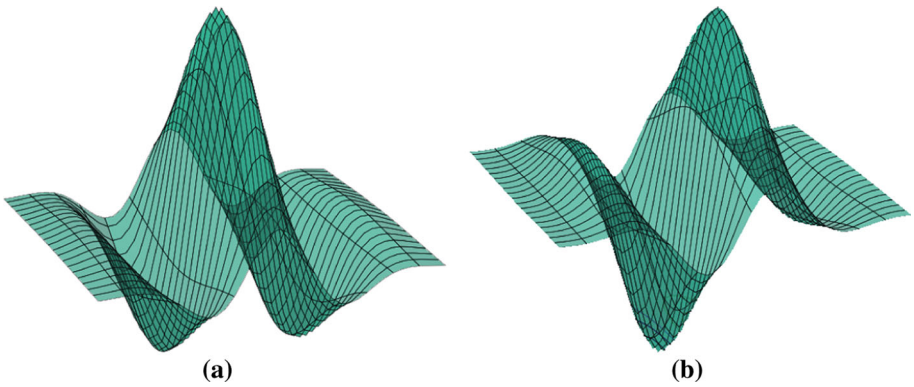

Fig. 1 2D Gabor functions in the spatial domain. **a** Real part, which is an even-symmetric function and **b** imaginary part that corresponds to an anti-symmetric function

$$g_o(x,y) = Ke^{-\frac{1}{2}\left(\frac{x^2+\gamma^2y^2}{\alpha^2}\right)}\sin(2\pi u_0 x) \tag{4}$$

is an odd-symmetric function. This function is ideal for detecting step-like discontinuities because it responds to zero-crossing [20].

The frequency response and orientation selectivity properties of Gabor functions are made explicit in the Fourier domain.

Consider that g_e is a pure-real even-symmetric function and its Fourier transform, $\mathcal{F}\{g_e\}$, is given by $\frac{1}{2}[\hat{G}(u,v) + \hat{G}(-u,-v)]$, which is a symmetric function about the Y-axis, whereas g_o is a pure-real odd-symmetric function and its Fourier transform, $\mathcal{F}\{g_o\}$, is $\frac{1}{2}[-i\hat{G}(u,v) + i\hat{G}(-u,-v)]$, which is a symmetric function around the origin. Note that if both even and odd parts are used, then they closely approximate to a Hilbert transform pair. Therefore, the Fourier transform of (2) is given by

$$\hat{G}(u,v) = e^{-2\pi^2\alpha^2\left[(\tilde{u}-u_0\cos\theta)^2+\frac{1}{\gamma^2}(\tilde{v}+u_0\sin\theta)^2\right]} \tag{5}$$

where $(\tilde{u},\tilde{v}) = (u\cos\theta, -u\sin\theta)$. This equation represents a rotated Gaussian function by an angle θ with u_0 frequency units shifted along the X-axis.

Psychophysical experiments have shown that frequency bandwidths of simple receptive fields are about one octave apart [1, 4]. To fulfill this condition, the half-amplitude bandwidth, B_u, of each filter was linked to its central frequency using

$$\alpha = \frac{\sqrt{\log(2)}(2^{B_u}+1)}{\sqrt{2}\pi u_0(2^{B_u}-1)} \tag{6}$$

where the central frequency is given in cycles/image-width.

If the central frequency is very small, then the filters will behave as low-pass filters rather than band-pass filters; this fact usually leads to a loss of information. Furthermore, there is an upper limit, $u \leq \frac{1}{2}$. Beyond this limit, the radial bandwidth, α, will be very large; thus, filtering may cause artifacts [17]. We selected the four following dyadic values $u = \{\sqrt{2}, 2\sqrt{2}, 4\sqrt{2}, 8\sqrt{2}\}$ to build an optimal filter bank with four scales.

In order to determine the optimal angular bandwidth, B_θ, we considered axisymmetric filters and set $\gamma = 1$

$$\frac{\alpha}{\gamma} = \frac{\sqrt{\log(2)}}{\sqrt{2}\pi u_0 \tan\left(\frac{B_\theta}{2}\right)} \tag{7}$$

in this way, $B_\theta \approx 36°$ but for computational efficiency $B_\theta = \frac{\pi}{6}$ was chosen. This setting resulted in a filter bank with six orientations, see (Fig. 2).

2.1 Gabor feature vectors

The goal of feature extraction is to identify similar characteristics or patterns that are common to a specific class. Such patterns may vary slightly within the class but they must be sensitive enough to discriminate elements from different classes. Gabor filters extract characteristics in specific orientations and frequency bands called complex Gabor coefficients denoted by $G_{(s,\theta)}$ and computed as follows:

$$G_{(s,\theta)}(x,y) = \sqrt{E^2_{(s,\theta)}(x,y) + O^2_{(s,\theta)}(x,y)} \tag{8}$$

with

$$\begin{aligned} E_{(s,\theta)} &= I \bigstar g_{e(s,\theta)} \\ O_{(s,\theta)} &= I \bigstar g_{o(s,\theta)} \end{aligned} \tag{9}$$

where I is the image and ★ indicates the convolution; $g_{o(s,\theta)}$ and $g_{e(s,\theta)}$ are the odd-symmetric and even-symmetric filters at the scale s and orientation θ, respectively.

Theoretically, the more the features, the greater the ability to discriminate images. Nevertheless, this statement is not always true because not all features are important for understanding or representing visual scenes [6].

We focused this study not only on energy signatures such as mean and standard deviation but also on higher-order statistics to increase the ability to extract characteristics. Since Gabor coefficients can be considered as

probability density functions, mean, standard deviation, skewness, and kurtosis are enough to provide a good approximation of a scene [21].

We investigated the following set of statistics, where M and N are the size of the coefficient.

- Mean

$$\mu_{(s,\theta)} = \frac{1}{NM}\sum_{x=1}^{N}\sum_{y=1}^{M} G_{(s,\theta)}(x,y) \tag{10}$$

- Standard deviation

$$\sigma_{(s,\theta)} = \sqrt{\frac{1}{NM}\sum_{x=1}^{N}\sum_{y=1}^{M}\left(G_{(s,\theta)}(x,y) - \mu_{(s,\theta)}\right)^2} \tag{11}$$

- Skewness (Υ) is a measure of asymmetry; it can be positive, which means that the distribution tends to the right, negative when the distribution tends to the left, or even zero, which typically implies a symmetric distribution:

$$\Upsilon_{(s,\theta)} = \frac{\mu^3_{(s,\theta)}}{\sigma^3_{(s,\theta)}} \tag{12}$$

We also included a measure of contrast (Ψ) using kurtosis (K)

$$\Psi_{(s,\theta)} = \frac{\sigma_{(s,\theta)}}{K^{0.25}_{(s,\theta)}} \tag{13}$$

where $K_{(s,\theta)} = \frac{\mu^4_{(s,\theta)}}{\sigma^4_{(s,\theta)}}$ represents the degree of peakedness of a distribution. We followed the recommendations in [27] and used 0.25 to reduce the contrast value when it comes distributions with biased peaks and to increase it with polarized distributions.

We used the four previous descriptors to characterize emphysema patterns and to construct Gabor Feature Vectors ($\overline{GFV}$) as follows:

$$\overline{GFV} = \left[\mu_{(0,0)}, \sigma_{(0,0)}, \Upsilon_{(0,0)}, \Psi_{(0,0)}, \ldots, \mu_{(s-1,\theta-1)}, \sigma_{(s-1,\theta-1)}, \Upsilon_{(s-1,\theta-1)}, \Psi_{(s-1,\theta-1)}\right] \tag{14}$$

2.2 Extended Gabor feature vectors with local binary patterns

LBPs have been successfully applied to texture classification. This approach is based on the idea that textural properties within homogeneous regions can be mapped into histograms that represent micro-features, see (Fig. 3).

Original LBP operator [18] uses a 3 × 3 square mask called "textum spectrum". The values within the mask that are smaller than the central pixel are replaced by "0" otherwise by "1". The new values are then multiplied by a fixed weighting function and summed to obtain the final label: $LBP(g_c) = \sum_{p=0}^{7} S(g_p - g_c)2^p$ where $\{g_p | p = 0, \ldots, 7\}$ are the neighbors of g_c, and the comparison function is defined as: $S(x) = \begin{cases} 1 & \text{if } x \geq 0 \\ 0 & \text{if } x < 0 \end{cases}$

Ojala et al. [19] improved their method by including a circular mask denoted by the subscript (P, R) where P is the number of sampling points and R is the radius of the neighborhood. If the sampling coordinates, $(x_p, y_p) = (x_c + R\cos(\frac{2\pi p}{P}), y_c - R\sin(\frac{2\pi p}{P}))$, do not fall at integer positions, then the values are bilinearly interpolated.

Furthermore, they observed that over 90 % of the patterns can be described with a few LBPs; so, they introduced a uniformity measure U that corresponds to changes (0/1) as follows:

$$U\left(LBP_{P,R}(g_c)\right) = |S(g_{P-1} - g_c) - S(g_0 - g_c)| + \sum_{p=1}^{P-1} |S(g_p - g_c) - S(g_{p-1} - g_c)| \tag{15}$$

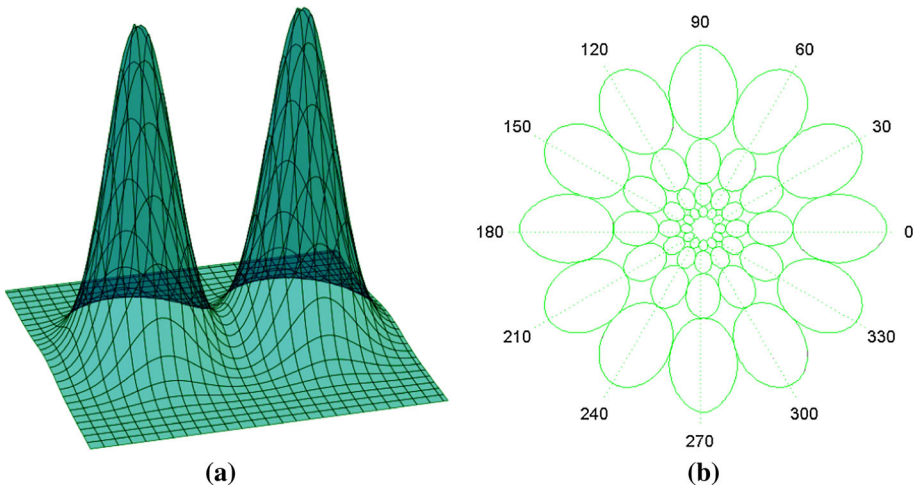

Fig. 2 Fourier transform of a 2D real Gabor function and its filter bank. **a** In the frequency domain, even-symmetric Gabor filters are represented by two real-valued Gaussian functions placed on each side of the origin symmetrically. **b** Contour lines of a real Gabor filter bank distributed in six orientations and four frequency bands. This filter bank was generated with the parameters proposed in this paper

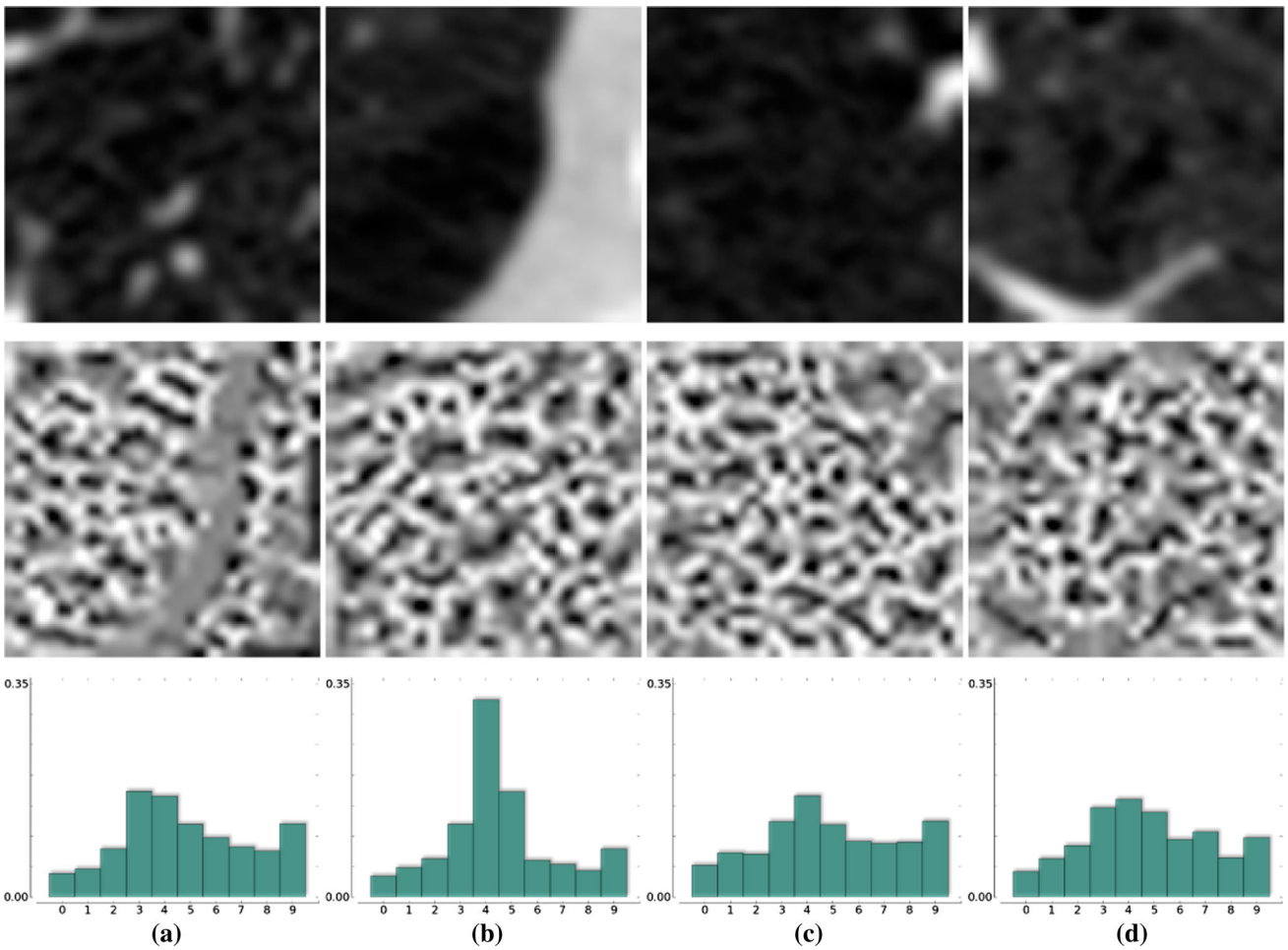

Fig. 3 Example of the $LBP^{uni}_{8,1}$ operator. The first row shows emphysema patches in the window $[-1000, -500]$ HU. The second row shows the labeled images, and the third row shows their histograms. All the images were magnified by a factor of 4 for a better visualization. **a** NT, **b** PS, **c** PL, and **d** CL

Thus, the uniform LBP ($LBP^{uni}_{P,R}$) can be obtained as:

$$LBP^{uni}_{p,R}(g_c) = \begin{cases} \sum_{p=0}^{p-1} S(g_p - g_c) & \textbf{if } U(LBP_{P,R}(g_c)) \\ \leq 2P+1 & \text{otherwise} \end{cases} \quad (16)$$

After this process is completed, a labeled image $L(x, y)$ is generated and the pixel-wise information is encoded as a histogram, H_i, so that it can be interpreted as a fingerprint or a signature of the analyzed object. $LBP^{uni}_{P,R}$ produces $(P + 2)$-bin histograms [16].

We propose to concatenate a $\overline{GFV}$ and its corresponding $LBP^{uni}_{P,R}$ histogram into a single sequence called extended Gabor feature vector ($\overline{EGFV}_{P,R}$) that represents any given texture patch.

$$\overline{EGFV}_{P,R} = \left[\overline{GFV}, H_i\right] \quad (17)$$

where

$$H_i = \sum_{x=1}^{N}\sum_{y=1}^{M} C\{L(x,y) == i | i = 0, \ldots, P+1\} \quad (18)$$

with

$$C(A) = \begin{cases} 1 & \textbf{if } \text{A is true} \\ 0 & \text{otherwise} \end{cases} \quad (19)$$

$\overline{EGFV}_{P,R}$ simultaneously encodes global texture characteristics extracted by Gabor filters and local information provided by LBPs.

3 Multi-class kernel Fisher discriminant analysis

It must be considered that the size of a training set should be exponentially increased with the dimensionality of the input space. Since our approach generates high-dimensional

vectors and a limited dataset is available, we used KFDA [15] that maps original data into a new feature space preventing overfitting. In addition, another motivation for reducing dimensionality is that psychophysical findings indicate that perceptual tasks such as similarity judgment tend to be performed on a low-dimensional representation [11].

Discriminant analysis was introduced by Ronald Fisher [7] for two-class problems (Fisher discriminant analysis, FDA) and remains to be one of the most popular methods for dimensionality reduction. Contrary to PCA, FDA projects vectors onto a line which preserves direction useful for data classification.

Nevertheless, FDA has an important limitation because it assumes Gaussian likelihoods. To overcome it, Mika et al. [15] proposed a nonlinear generalization by mapping original data into some space ζ in order to compute FDA there.

The goal is to find $w^* \in \zeta$ that maximizes

$$J(w) = \frac{w^T \boldsymbol{S}_B^{\Phi} w}{w^T \boldsymbol{S}_W^{\Phi} w} \tag{20}$$

where $\boldsymbol{S}_B^{\Phi}$ and $\boldsymbol{S}_W^{\Phi}$ are the corresponding matrices in ζ.

Let $\boldsymbol{X}^1 = \{x_1^1, x_2^1, \ldots, x_{l_1}^1\}, \ldots, \boldsymbol{X}^C = \{x_1^C, x_2^C, \ldots, x_{l_C}^C\}$ be feature vectors from C classes, it is necessary to define a matrix form of the inner product $k(x,y) = \langle \boldsymbol{\Phi}(x), \boldsymbol{\Phi}(y) \rangle$. The idea is to compute dot products of mapped data without a mapping function; thus, the kernel matrix is defined as: $\boldsymbol{K}(m,n) = k(X_m, X_n)$ where $\boldsymbol{X} = \bigcup_{i=1}^{C} \boldsymbol{X}^i$.

There are three popular kernels functions: (i) polynomial, $k(x,y) = (xy + a)^b$; (ii) sigmoidal, $k(x,y) = \tanh(axy + b)$; and (iii) Gaussian or Radial Basis Function (RBF), $k(x,y) = e^{-\frac{1}{2}\frac{\|x-y\|^2}{a^2}}$. For all kernels $a, b \in \mathbb{R}^+$.

It follows that

$$\begin{aligned} w^T \boldsymbol{S}_B^{\Phi} w &= \alpha \boldsymbol{P} \alpha^T \\ w^T \boldsymbol{S}_W^{\Phi} w &= \alpha \boldsymbol{Q} \alpha^T \end{aligned} \tag{21}$$

Now, the between-class scatter matrix is defined by

$$\boldsymbol{P} = \sum_{j=1}^{C} l_j (\mu_j - \mu)(\mu_j - \mu)^T \tag{22}$$

where $\mu_j = \frac{1}{l_j} \sum_{\forall n \in X^j} \boldsymbol{K}(m,n)$ and $\mu = \frac{1}{l} \sum_{\forall n} \boldsymbol{K}(m,n)$.

$\boldsymbol{Q}$ is the within-class scatter matrix defined by:

$$\boldsymbol{Q} = \boldsymbol{K}\boldsymbol{K}^T - \sum_{j=1}^{C} l_j \mu_j \mu_j^T \tag{23}$$

$\boldsymbol{Q} = \boldsymbol{Q} + r\boldsymbol{I}$ to guarantee that $\boldsymbol{Q}$ is positive definite.

Finally, α^* is built with the $C - 1$ largest eigenvalues of $\boldsymbol{Q}^{-1}\boldsymbol{P}$, and the projection can be computed as:

$$y = \boldsymbol{K}\alpha^* \tag{24}$$

Note that this method reduces the length of $\overline{EGFV}_{P,R}$ to $C - 1$ bins.

4 Material

We used two datasets labeled by experienced pulmonologists. The **Bruijne and Sørensen (BS) dataset** was provided by Prof. Dr. Bruijne and Dr. Sørensen [24]. It consists of 168 non-overlapping patches of size 61 × 61 pixels manually annotated in 25 subjects previously divided into three groups: healthy non-smokers, smokers without COPD, and smokers with moderate or severe COPD. These patches belong to three patterns: NT (59 patches from 8 subjects), CL (50 patches from 7 subjects), and PS (59 patches from 10 subjects). The NT patches were annotated in healthy non-smokers, while the CL and PS patches were annotated in both smokers with and without COPD.

Brigham and Women's Hospital (BWH) dataset was provided by the Brigham and Women's Hospital using a subset of the COPDGene study [13, 29]. The COPDGene study uses 342 CT scanners located in 16 different sites. In total, 1337 patches that belong to 353 subjects were randomly selected. The distribution per pattern is as follows: NT (370 patches from 74 subjects), PS (184 patches from 52 subjects), and PL (148 patches from 39 subjects). In addition, BWH includes three subtypes of CL (mild, moderate, and severe): CL1 (170 patches from 5 subjects), CL2 (287 patches from 84 subjects), and CL3 (178 patches from 49 subjects), respectively. The size of the samples was chosen to fit the physical extent of emphysema within the secondary lobule corresponding to 31 × 31 pixels. Prior to the application of our approach, the data were normalized by the global mean and the standard deviation. Neither BS nor BHW contains private information of patients.

5 Experiments and results

Parameter selection is a fundamental step in any classification problem; its goal is to find a global optimum to achieve the best results in terms of accuracy and bias.

Tenfold cross-validation is a simple and yet widely employed technique for model validation that randomly splits up data into 10 disjoint subsets of approximately equal size. For each fold, the remaining nine subsets are used to train the model then the average of all folds should provide an estimate of the model. However, in order to reduce bias, Varma et al. [28] recommend a nested procedure that divides the data into tenfolds, for each fold, the

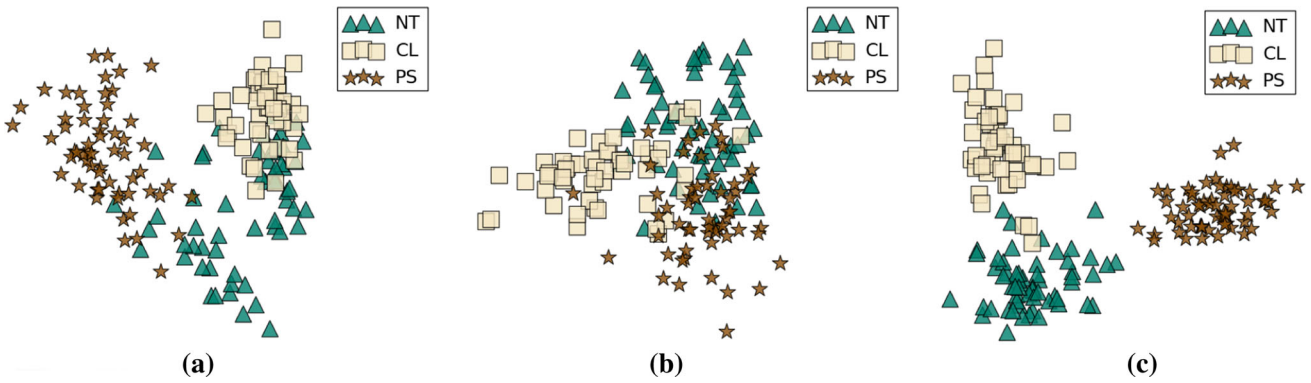

Fig. 4 KFDA on the BS three-class dataset. The data were reduced into a 2D space. The vectors were produced by **a** $\overline{GFV}$ (96-dimensional space); **b** $LBP^{uni}_{P,R}$ (10-dimensional space); and **c** $\overline{EGFV}_{8,1}$ (109-dimensional space). The final space depends on the number of classes

remaining nine subsets are divided into ten subsets to train the model.

It is important that any method generalizes to unseen patients; thus, a solution is to use only a single patch of each patient. Leave-one-patient-out cross-validation divides the original dataset such that each partition contains only samples of a single patient.

In order to assess our approach, we used the proposal of Varma et al. with the parameters found in the inner circle of the cross-validation that maximized the average accuracy. We also assessed the full datasets with leave-one-patient-out cross-validation. In the classification stage, we used k-NN classifier and the Euclidean distance as a metric; such a distance was computed from the input samples to every training data, so that we classified the samples using the majority rule among the k-closest vectors.

5.1 BS dataset

This dataset was previously presented in [24] where the authors achieved the best classification rate using $k = 1$ in the k-NN classifier. We completed several tests varying $k = \{1, 2, \ldots, 25\}$, and the best rate was achieved with $k = 20$. Since KFDA projects data onto a new space where class separation is maximized, the rate variation due to changes in k was minimized, see (Fig. 4). We used the RBF kernel with $a = 543$, the classification rates in the range $a < 450$ and $a > 550$ decreased dramatically due to the variance of the kernel.

We tested three combinations of $\overline{GFV}$ and $LBP^{uni}_{P,R}$ by varying the number of neighbors and radius length: {8, 1}, {16, 2}, and {24, 3}. These values are recommended in the literature for testing purposes [19]. Furthermore, we computed precision (Pr), sensitivity (Se), and F_1-Score $= 2 \times \frac{\mathrm{Pr} \times \mathrm{Se}}{\mathrm{Pr} + \mathrm{Se}}$, which is a measure of accuracy and reaches its best value at 1 and worst score at 0.

The results using tenfold cross-validation were summarized in Table 1. The highest precision rate, 93.70 %, was achieved using $\overline{EGFV}_{16,2}$, which is a combination of $\overline{GFV}$ and $LBP^{uni}_{16,2}$. We set the radius length at $R = 2$, which led to a higher accuracy of about 6 %. On the contrary, $R > 2$ caused lower accuracies. This fact suggests that local variations, which can be interpreted as edges, may be useful for characterizing emphysema patterns. We also increased the number of neighbors, $P = 16$, that made our approach less sensitive to noise because there are more neighbors to average; however, it may cause over-smoothing with larger values of P.

Furthermore, we carried out a comparison of the methods $\overline{GFV}$, $LBP^{uni}_{8,1}$, $LBP^{uni}_{16,2}$, and $LBP^{uni}_{24,3}$. We also computed the performance of Gabor filters using only the real part, see (8). The estimated classification rates are shown in Table 2.

Table 3 summarizes comparisons between $\overline{GFV}$, $LBP^{uni}_{P,R}$, and $R_{(s,\theta)}$, which are distinguished as "single descriptors" and $\overline{EGFV}_{P,R}$, distinguished as "extended descriptor." The classification rates were achieved using leave-one-patient-out cross-validation. It is worth mentioning that although Sørensen et al. used the same dataset, a straightforward comparison is not possible because they did not report classification rates for patches of 61 × 61 pixels.

5.2 BWH dataset

The BWH dataset was previously used in [13] where the authors achieved a precision of 66 %. Also in [29], the dataset was used with a technique based on an embedded probabilistic PCA that resulted in a precision of 69 %. Note that this dataset includes three subtypes of CL (mild, moderate, and severe), which increase the complexity of the classification task.

Table 1 Classification results of $\overline{EGFV}_{8,1}$, $\overline{EGFV}_{16,2}$, and $\overline{EGFV}_{24,3}$ with the BS dataset and tenfold cross-validation

	$\overline{EGFV}_{8,1}$				$\overline{EGFV}_{16,2}$				$\overline{EGFV}_{24,3}$			
	NT	CL	PS	Mean (±SD)	NT	CL	PS	Mean (±SD)	NT	CL	PS	Mean (±SD)
Pr	81.03	88.00	90.00	86.34 (±4.71)	88.71	95.83	96.55	**93.70** (±4.33)	78.69	89.36	88.33	85.46 (±5.89)
Se	79.66	88.00	91.53	86.40 (±6.10)	93.22	92.00	94.92	**93.38** (±1.47)	81.36	84.00	89.83	85.06 (±4.34)
F_1-Score	80.34	88.00	90.76	86.37 (±5.40)	90.91	93.88	95.73	**93.51** (±2.43)	80.00	86.60	89.07	85.22 (±4.69)

All the data are expressed in (%)

Bold values represent the best rates achieved by the corresponding descriptor

$\overline{EGFV}_{PR}$ extended Gabor feature vector with P sampling points and radius R

Table 2 Comparison of the methods $\overline{GFV}$, $LBP^{uni}_{P,R}$, and $\overline{R_{(s,\theta)}}$ using the BS dataset and tenfold cross-validation

Descriptor	Pr				Se				F_1-Score
	NT	CL	PS	Mean (±SD)	NT	CL	PS	Mean (±SD)	
$LBP^{uni}_{8,1}$	68.85	79.59	74.14	74.19 (±5.37)	71.19	78.00	72.88	74.02 (±3.54)	74.11
$LBP^{uni}_{16,2}$	74.60	79.59	82.14	**78.78** (±3.84)	79.66	78.00	77.97	**78.54** (±0.97)	**78.66**
$LBP^{uni}_{24,3}$	73.33	85.11	77.05	78.49 (±6.02)	74.58	80.00	79.66	78.08 (±3.04)	78.28
$\overline{GFV}$	70.37	75.00	87.10	77.49 (±8.64)	64.41	78.00	91.53	77.98 (±13.56)	77.73
$\overline{R_{(s,\theta)}}$	65.38	71.15	84.38	73.64 (±9.74)	57.63	74.00	91.53	74.39 (±16.95)	74.01

All the data are expressed in (%)

Bold values represent the best rates achieved by the corresponding descriptor

$\overline{R_{(s,\theta)}}$ Gabor feature vectors using only real filters, $\overline{GFV}$ Gabor feature vector, LBP^{uni}_{PR} local binary pattern with P sampling points and radius R

Table 3 Comparison rates in the BS dataset using leave-one-patient-out cross-validation

	Descriptor	Pr				Se				F_1-Score
		NT	CL	PS	Mean (±SD)	NT	CL	PS	Mean (±SD)	
Single	$LBP^{uni}_{8,1}$	61.40	76.60	67.19	68.40 (±7.67)	59.32	72.00	72.88	68.07 (±7.58)	68.24
	$LBP^{uni}_{16,2}$	74.58	76.60	75.81	75.66 (±1.09)	74.58	72.00	79.66	75.41 (±3.90)	75.54
	$LBP^{uni}_{24,3}$	69.84	82.61	77.97	**76.80** (±6.46)	74.58	76.00	77.97	**76.18** (±1.70)	**76.49**
	$\overline{GFV}$	53.33	64.44	82.54	66.77 (±14.74)	54.24	58.00	88.14	66.79 (±18.58)	66.78
	$\overline{R_{(s,\theta)}}$	57.41	66.00	82.81	68.74 (±12.92)	52.54	66.00	89.83	69.46 (±18.88)	69.10
Extended	$\overline{EGFV}_{8,1}$	77.19	87.76	85.48	83.48 (±5.56)	74.58	86.00	89.83	83.47 (±7.93)	83.48
	$\overline{EGFV}_{16,2}$	83.87	93.48	91.67	**89.67** (±5.10)	88.14	86.00	93.22	**89.12** (±3.70)	**89.39**
	$\overline{EGFV}_{24,3}$	80.00	87.23	90.16	85.89 (±5.23)	81.36	82.00	93.22	85.53 (±6.67)	85.71

All the data are expressed in (%)

Bold values represent the best rates achieved by the corresponding descriptor

$\overline{R_{(s,\theta)}}$ Gabor feature vectors using only real filters, $\overline{GFV}$ Gabor feature vector, LBP^{uni}_{PR} local binary pattern with P sampling points and radius R, $\overline{EGFV}_{PR}$ extended Gabor feature vector with P sampling points and radius R

The results using the BWH dataset and tenfold cross-validation are summarized in Table 4. We kept the previous configuration, $k = 20$ and the RBF kernel with $a = 543$ and also assessed three possible combinations of $\overline{GFV}$ and $LBP^{uni}_{P,R}$. The best precision was achieved with $\overline{EGFV}_{16,2}$.

We carried out a comparison among the methods: $\overline{GFV}$, $LBP^{uni}_{8,1}$, $LBP^{uni}_{16,2}$, $LBP^{uni}_{24,3}$, and $\overline{R_{(s,\theta)}}$. The estimated rates are shown in Table 5. Note that all the single descriptor rates were lower than those obtained by our approach.

We summarized in Table 6 comparisons of all the previous methods using leave-one-patient-out cross-validation. The best rate was achieved with our approach, $\overline{EGFV}_{16,2}$. Note that when it comes BWH, the variance is larger than in

Table 4 Classification rates of $\overline{EGFV}_{8,1}$, $\overline{EGFV}_{16,2}$, and $\overline{EGFV}_{24,3}$ using the BWH dataset and tenfold cross-validation

	$\overline{EGFV}_{8,1}$							$\overline{EGFV}_{16,2}$							$\overline{EGFV}_{24,3}$						
	NT	PS	PL	CL1	CL2	CL3	Mean (±SD)	NT	PS	PL	CL1	CL2	CL3	Mean (±SD)	NT	PS	PL	CL1	CL2	CL3	Mean (±SD)
Pr	77.43	83.42	73.03	58.20	63.11	57.69	68.81 (±10.72)	80.79	85.28	78.23	65.25	62.54	61.64	**72.29** (±10.34)	79.27	86.63	78.01	56.72	60.62	57.93	69.86 (±12.94)
Se	86.22	87.50	75.00	41.76	72.13	42.13	67.46 (±20.66)	88.65	91.30	77.70	45.29	70.38	50.56	**70.65** (±19.22)	87.84	88.04	74.32	44.71	67.60	47.19	68.28 (±19.03)
F_1-Score	81.91	85.41	74.00	48.63	67.32	48.70	67.66 (±16.00)	84.54	88.19	77.96	53.47	66.23	55.55	**71.00** (±14.81)	83.34	87.33	76.12	50.00	63.92	52.01	68.79 (±15.92)

All the data are expressed in (%)

Bold values represent the best rates achieved by the corresponding descriptor

$\overline{EGFV}_{PR}$ extended Gabor feature vector with P sampling points and radius R

Table 5 Comparisons among $\overline{GFV}$, $LBP^{uni}_{P,R}$, and $\overline{R_{(s,\theta)}}$ using the BWH dataset and tenfold cross-validation

Descriptor	Pr							Se							F_1-Score
	NT	PS	PL	CL1	CL2	CL3	Mean (±SD)	NT	PS	PL	CL1	CL2	CL3	Mean (±SD)	
$LBP^{uni}_{8,1}$	57.46	70.56	61.54	29.85	54.67	33.01	51.18 (±16.25)	77.03	82.07	43.24	11.76	67.25	19.10	50.08 (±30.07)	50.62
$LBP^{uni}_{16,2}$	58.17	80.09	57.47	36.26	55.26	29.81	52.84 (±17.91)	78.92	91.85	33.78	19.41	65.85	17.42	51.21 (±31.91)	52.01
$LBP^{uni}_{24,3}$	59.74	84.74	58.25	30.65	52.87	29.09	52.56 (±20.74)	74.59	87.50	40.54	22.35	64.11	17.98	51.18 (±28.57)	51.86
$\overline{GFV}$	70.55	79.05	72.90	44.71	52.40	55.56	**62.53** (±13.52)	80.27	90.22	76.35	22.35	57.14	47.75	**62.35** (±25.04)	**62.44**
$\overline{R_{(s,\theta)}}$	70.00	78.10	69.09	51.81	51.30	53.90	62.37 (±11.46)	81.35	89.13	77.03	25.29	55.05	42.70	61.76 (±24.92)	62.06

All the data are expressed in (%)

Bold values represent the best rates achieved by the corresponding descriptor

$\overline{R_{(s,\theta)}}$ Gabor feature vectors using only real filters, $\overline{GFV}$ Gabor feature vector, LBP^{uni}_{PR} local binary pattern with P sampling points and radius R

Table 6 Comparison rates using the BWH dataset and leave-one-patient-out cross-validation

Descriptor	Pr						Se						F_1-Score
	NT	PL	PS	CL1	CL2	CL3	Mean (±SD)	NT	PL	PS	CL1	CL2	CL3	Mean (±SD)	
Single															
$LBP^{uni}_{8,1}$	55.89	68.49	58.04	26.09	52.16	26.53	47.87 (±17.56)	74.32	81.52	43.92	10.59	63.07	14.61	48.01 (±30.25)	47.94
$LBP^{uni}_{16,2}$	57.65	79.90	51.76	32.97	55.46	31.52	51.54 (±17.90)	78.38	90.76	29.73	17.65	68.99	16.29	50.30 (±32.93)	50.91
$LBP^{uni}_{24,3}$	58.95	82.81	57.01	29.32	55.39	30.77	52.38 (±19.99)	72.97	86.41	41.22	22.94	66.20	17.98	51.29 (±28.07)	51.83
$\overline{GFV}$	69.72	79.43	69.62	41.05	51.15	50.00	**60.17** (±14.85)	80.27	90.22	74.32	22.94	54.36	40.45	**60.43** (±25.76)	**60.30**
$\overline{R_{(s,\theta)}}$	68.69	77.36	72.26	34.57	49.17	50.00	58.68 (±16.62)	79.46	89.13	75.68	16.47	51.57	44.94	59.54 (±27.07)	59.11
Extended															
$\overline{EGFV}_{8,1}$	77.94	84.26	73.47	59.17	62.15	54.29	68.55 (±11.76)	85.95	90.22	72.97	41.76	70.38	42.70	67.33 (±20.84)	67.94
$\overline{EGFV}_{16,2}$	80.84	85.35	77.33	60.34	61.76	59.86	**70.91** (±11.54)	88.92	91.85	78.38	41.18	68.64	49.44	**69.74** (±20.79)	**70.32**
$\overline{EGFV}_{24,3}$	78.61	87.30	77.08	52.31	59.94	58.16	68.90 (±13.93)	88.38	89.67	75.00	40.00	66.20	46.07	67.55 (±20.98)	68.22

All the data are expressed in (%)

The bold values represent the best rates achieved by the corresponding descriptor

$\overline{R_{(s,\theta)}}$ Gabor feature vectors using only real filters, $\overline{GFV}$ Gabor feature vector, LBP^{uni}_{PR} local binary pattern with P sampling points and radius R, $\overline{EGFV}_{PR}$ extended Gabor feature vector with P sampling points and radius R

BS because BWH includes three subtypes of CL. Since low-attenuation areas in CL may vary in shape, some patients show well-defined borders patterns, while others do not. Therefore, CL is not a single morphological feature.

6 Conclusions

In this paper, we proposed a new approach to quantify up to six emphysema patterns based on complex Gabor filters and local binary patterns. This joint model allows to encode global texture characteristics with local information simultaneously. We presented the complex Gabor model and summarized its properties related to the human visual system. Since Gabor-based methods transform images into a high-dimensional feature vectors, we applied kernel Fisher discriminant analysis via the kernel trick to avoid computing a mapping function and to find discriminant boundaries among classes. Then, we performed tenfold cross-validation and leave-one-patient-out cross-validation to assess our approach.

We also included a comparison between complex and real Gabor filters. The difference is that in the frequency, domain real Gabor filters are represented by two real-valued Gaussians symmetrically placed on each side of the origin, whereas complex Gabor filters are represented with a single Gaussian on the positive side of the spectrum. Therefore, real filters contain more redundant information than complex filters. However, redundant information does not always allow greater discrimination ability. This suggests that the next step to improve the classification should be a sparse model that performs a deeper analysis of the redundant information.

In general, the extended descriptors increased precision rates around 15 % in the BW dataset. Concerning the BWH dataset, our method achieved a F_1 score of 70.32, which means 10 % above any single descriptor. Theses results were mainly influenced by the misclassified severity levels of CL, most of the errors occurred between moderate and severe emphysema that could indicate a limitation of the BWH database.

It seems that only the distribution of attenuation values in PS is clearly different from the rest of the classes. Since we consider that the main limitation of filter approaches is that the information from each coefficient is represented with a few moments causing loss of information in terms of orientation and distribution, we used LBPs to overcome this limitation and characterize the distributions of local patterns. Most of the errors using $\overline{GFV}$ occurred between NT and CL patterns but the precision rates of such patterns increase around 30 % when $\overline{EGFV}_{16,2}$ is used. These results have shown that the proposed approach is a promising technique that yields a good performance in

emphysema classification and successfully discriminates among NT, CL, PL, and PS in CT images. Its value lies in providing an independent quantification of the disease in order to propose new therapies. Furthermore, this approach may be useful in other textural classification scenarios beyond medical imaging.

Acknowledgments This work has been partially sponsored by the grants UNAM PAPIIT IN113611, IG100814, and TEC2010-20307 from the Spanish Ministry of Economy. R. Nava gives a special thank to Consejo Nacional de Ciencia y Tecnología for the doctoral scholarship 167161. R. San José Estépar is supported by NIH grants K25 HL104085-03 and 1R01HL116931-01. We extend our gratitude to Prof. Dr. Marleen de Bruijne and Dr. Lauge Sørensen from the Department of Computer Science (DIKU) at University of Copenhagen for sharing their lung database. The authors also thank Madrid-MIT M+Visión Consortium for its support to make this research work possible and to the COPDGene study for the contribution of the data.

References

1. Bovik AC, Clark M, Geisler WS (1990) Multichannel texture analysis using localized spatial filters. IEEE Trans Pattern Anal Mach Intell 12(1):55–73
2. Brody H (2012) Chronic obstructive pulmonary disease. Nature 489(7417):S1
3. Costa AF, Humpire-Mamani G, Traina AJM (2012) An efficient algorithm for fractal analysis of textures. In: 25th Conference on graphics, patterns, and images (SIBGRAPI), 39–46
4. Daugman JG (1985) Uncertainty relation for resolution in space, spatial frequency, and orientation optimized by two-dimensional visual cortical filters. J Opt Soc Am A 2(7):1160–1169
5. Depeursinge A, Foncubierta-Rodríguez A, Ville D, Müller H (2012) Multiscale lung texture signature learning using the Riesz transform. In: Medical image computing and computer-assisted intervention, *Lecture Notes in Computer Science*, vol 7512, pp 517–524. Springer, Berlin
6. ElAlami ME (2011) A novel image retrieval model based on the most relevant features. Knowl-Based Syst 24(1):23–32
7. Fisher RA (1936) The use of multiple measurements in taxonomic problems. Ann Euge 7(2):179–188
8. Gabor D (1946) Theory of communication. J Inst Elec Eng (London) 93III:429–457
9. Hayhurst M, Flenley DC, Mclean A, Wightman AJA, Macnee W, Wright D, Lamb D, Best J (1984) Diagnosis of pulmonary emphysema by computerised tomography. The Lancet 324(8398):320–322
10. Hubel DH, Wiesel TN (2005) Brain and visual perception: the story of a 25-year collaboration. Oxford University Press, New York
11. Liu C, Wechsler H (2002) Gabor feature based classification using the enhanced Fisher linear discriminant model for face recognition. IEEE Trans Image Process 11(4):467–476
12. Madani A, Zanen J, de Maertelaer V, Gevenois PA (2006) Pulmonary emphysema: objective quantification at multi-detector row CT-comparison with macroscopic and microscopic morphometry. Radiology 238(3):1036–1043
13. Mendoza CS, Washko GR, Ross JC, Diaz AA, Lynch DA, Crapo JD, Silverman EK, Acha B, Serrano C, Estépar RS (2012) Emphysema quantification in a multi-scanner HRCT cohort using local intensity distributions. In: 9th IEEE International symposium on biomedical imaging, pp 474–477
14. Mets OM, Jong PA, van Ginneken B, Gietema HA, Lammers JW (2012) Quantitative computed tomography in COPD: possibilities and limitations. Lung 190(2):133–145
15. Mika S, Ratsch G, Weston J, Scholkopf B, Muller K Fisher (1999) discriminant analysis with kernels. In: Proceedings of the 1999 IEEE signal processing society workshop. Neural Networks for Signal Processing IX, pp 41–48,
16. Nava R, Cristóbal G, Escalante-Ramŕez B (2012) A comprehensive study of texture analysis based on local binary patterns. In: Proceedings of SPIE 8436, optics, photonics, and digital technologies for multimedia applications II, pp 84–95
17. Nava R, Escalante-Ramírez B, Cristóbal G (2012) Texture image retrieval based on log-Gabor features. In: Progress in pattern recognition, image analysis, computer vision, and applications, *Lecture Notes in Computer Science*, vol 7441, pp 414–421. Springer, Berlin
18. Ojala T, Pietikäinen M, Harwood D (1994) Performance evaluation of texture measures with classification based on Kullback discrimination of distributions. In: Proceedings of the 12th international conference on pattern recognition—conference A: computer vision image processing (IAPR), vol 1, pp 582–585,
19. Ojala T, Pietikäinen M, Maenpaa T (2002) Multiresolution gray-scale and rotation invariant texture classification with local binary patterns. IEEE Trans Pattern Anal Mach Intell 24(7):971–987
20. Redondo R, Šroubek F, Fischer S, Cristóbal G (2009) Multifocus image fusion using the log-Gabor transform and a multisize windows technique. Inf Fusion 10(2):163–171
21. Schwartz WR, Roberti de Siqueira F, Pedrini H (2012) Evaluation of feature descriptors for texture classification. J Electron Imaging 21(2):0230016-1–023016-17
22. Sin DD (2012) Mortality in COPD: the role of comorbidities. In: Chronic obstructive pulmonary disease, respiratory medicine. Humana Press, pp 1–13
23. Sørensen L, Nielsen M, Lo P, Ashraf H, Pedersen, JH, de Bruijne M (2012) Texture-based analysis of COPD: a data-driven approach. IEEE Trans Med Imaging 31(1):70–78
24. Sørensen L, Shaker SB, de Bruijne M (2010) Quantitative analysis of pulmonary emphysema using local binary patterns. IEEE Trans Med Imaging 29(2):559–569
25. Sverzellati N, Randi G, Spagnolo P, Marchianò A, Silva M (2013) Increased mean lung density: another independent predictor of lung cancer? Eur J Radiol 82(8):1325–1331
26. Takahashi M, Fukuoka J, Nitta N, Takazakura R, Nagatani Y, Murakami Y, Otani H, Murata K (2008) Imaging of pulmonary emphysema: a pictorial review. Int J Chron Obstruct Pulmon Dis 3(2):193–204
27. Tamura H, Mori S, Yamawaki T (1978) Textural features corresponding to visual perception. IEEE Trans Syst Man Cybern 8(6):460–473
28. Varma S, Simon R (2006) Bias in error estimation when using cross-validation for model selection. BMC Bioinformatics 7(1):91–98
29. Zulueta-Coarasa T, Kurugol S, Ross J, Washko G, Estepar RS (2013) Emphysema classification based on embedded probabilistic PCA. In: Proceedings of the 35th annual international conference of the IEEE engineering in medicine and biology society, pp 3969–3972